The Astronomical Journal, 140:184–195, 2010 July doi:10.1088/0004-6256/140/1/184

DOUBLE-LINED SPECTROSCOPIC BINARY STARS IN THE RAVE SURVEY

G. Matijevič[1], T. Zwitter[1,2], U. Munari[3], O. Bienaymé[4], J. Binney[5], J. Bland-Hawthorn[6], C. Boeche[7], R. Campbell[8], K. C. Freeman[9], B. Gibson[10], G. Gilmore[11], E. K. Grebel[12], A. Helmi[13], J. F. Navarro[14], Q. A. Parker[15], G. M. Seabroke[16], A. Siebert[4], A. Siviero[3,7], M. Steinmetz[7], F. G. Watson[17], M. Williams[7], and R. F. G. Wyse[18]

[1] Faculty of Mathematics and Physics, University of Ljubljana, Ljubljana, Slovenia; gal.matijevic@fmf.uni-lj.si
[2] Center of Excellence SPACE-SI, Ljubljana, Slovenia
[3] INAF Osservatorio Astronomico di Padova, Asiago, Italy
[4] Observatorie de Strasbourg, Strasbourg, France
[5] Rudolf Pierls Center for Theoretical Physics, University of Oxford, Oxford, UK
[6] Sydney Institute for Astronomy, School of Physics, University of Sydney, Sydney, Australia
[7] Astrophysikalisches Institut Potsdam, Potsdam, Germany
[8] Western Kentucky University, Bowling Green, KY, USA
[9] RSAA, Australian National University, Camberra, Australia
[10] University of Central Lancashire, Preston, UK
[11] Institute of Astronomy, Cambridge, UK
[12] Astronomisches Rechen-Institut, Zentrum für Astronomie der Universität Heidelberg, Heidelberg, Germany
[13] Kapteyn Astronomical Institute, University of Groningen, Groningen, The Netherlands
[14] University of Victoria, Victoria, Canada
[15] Macquarie University, Sydney, Australia
[16] e2v Centre for Electronic Imaging, Planetary and Space Sciences Research Institute, The Open University, Walton Hall, Milton Keynes, UK
[17] Anglo-Australian Observatory, Sydney, Australia
[18] John Hopkins University, Baltimore, MD, USA
Received 2010 March 3; accepted 2010 May 17; published 2010 June 8

ABSTRACT

We devise a new method for the detection of double-lined binary stars in a sample of the Radial Velocity Experiment (RAVE) survey spectra. The method is both tested against extensive simulations based on synthetic spectra and compared to direct visual inspection of all RAVE spectra. It is based on the properties and shape of the cross-correlation function, and is able to recover ∼80% of all binaries with an orbital period of order 1 day. Systems with periods up to 1 yr are still within the detection reach. We have applied the method to 25,850 spectra of the RAVE second data release and found 123 double-lined binary candidates, only eight of which are already marked as binaries in the SIMBAD database. Among the candidates, there are seven that show spectral features consistent with the RS CVn type (solar type with active chromosphere) and seven that might be of W UMa type (over-contact binaries). One star, HD 101167, seems to be a triple system composed of three nearly identical G-type dwarfs. The tested classification method could also be applicable to the data of the upcoming *Gaia* mission.

Key words: binaries: spectroscopic – methods: data analysis – surveys

1. INTRODUCTION

Double-lined spectroscopic binaries, and in particular their eclipsing variants (EB-SB2s), are important astrophysical testbeds that provide a wealth of constraints on stellar models. EB-SB2s are the primary provider of accurate stellar masses and radii. When coupled with accurate atmospheric temperatures, the orbital solution of EB-SB2s geometrically fixes distance with great accuracy, becoming a critical testbed even for *Hipparcos* astrometric parallaxes (e.g., the case of the Pleiades cluster; Munari et al. 2004; van Leeuwen 2007, and references therein). If the components of a binary were born together, then they lie on the same isochrone. This constrains their metallicity and stellar models that reproduce them, including recent refinements such as the efficiency of overshooting and the role of atmospheric sedimentation of heavy elements (e.g., Tomasella et al. 2008). Torres et al. (2009) provide a recent and updated review of astrophysical results based on the study of binaries.

The Radial Velocity Experiment (RAVE) is an ongoing multi-fiber spectroscopic survey based on the UK Schmidt Telescope at the Anglo Australian Observatory. With a goal of observing 1 million stars, the survey has so far gathered more than 400,000 spectra in the magnitude range between $9 < I_C < 13$. The wavelength range of spectra covers the near-infrared (near-IR) interval from 8400 Å to 8800 Å with a resolving power of ∼7500, typically with a high signal-to-noise ratio (S/N; mean value of 45). This range is virtually free from any telluric lines. The Doppler shift of the lines permits us to measure the radial velocity to a precision of 1.3 km s^{-1}, and several prominent metallic and hydrogen spectral lines make it possible to derive accurate stellar atmospheric parameters and chemical composition (see Zwitter et al. 2004; Boeche et al. 2010 for more details). So far two data releases have been published (Steinmetz et al. 2006; Zwitter et al. 2008, hereafter Z08), and a third one will soon be released (A. Siebert et al. 2010, in preparation).

The primary goal of the RAVE survey is to measure precise radial velocities and atmospheric parameters of up to a million normal single stars with known proper motions and photometric data. The atmospheric parameters are used to infer the absolute magnitude and to estimate the distance to the targets (Breddels et al. 2010; T. Zwitter et al. 2010, in preparation). This in turn fixes all six phase-space coordinates and Galactic orbits. When coupled with information on metallicity and chemical abundances (which RAVE also provides), the RAVE survey is well suited to investigate Galactic structure and dynamics (Smith et al. 2007; Seabroke et al. 2008; Siebert et al. 2008; Veltz et al. 2008).

The unbiased sample of input stars selected for RAVE also includes, of course, a minority of peculiar and spectroscopic binary stars. The ability of RAVE spectra to identify and

properly characterize spectra with special features has already been demonstrated by the study of luminous blue variable supergiants in the Large Magellanic Cloud (Munari et al. 2009) and diffuse interstellar bands over the RAVE wavelength range (Munari et al. 2008). Double-lined binary stars are not specifically tackled by the RAVE main analysis pipeline. The aim of this paper is to discuss a tool parallel to the main pipeline to identify double-lined binary star candidates (and to distinguish them from other types of peculiar stars, in particular those showing emission-line cores), and to derive the radial velocity and atmospheric parameters of both components. The analysis is carried out on the RAVE second data release. Single-lined binaries collected from repeated observations will be treated in a separate paper. Section 2 discusses the SB2 detection method, based on the shape of the cross-correlation function (CCF). In Section 3, we evaluate the performance of our method on a sample of synthetic binary spectra. Two tables in Section 4 list all the binary candidates we have discovered among RAVE stars from the second data release, along with radial velocities and effective temperatures of both components.

2. CLASSIFICATION OF PECULIAR SPECTRA

The identification of all peculiar and SB2 spectra in the RAVE survey is relevant because (1) it cleans the survey products from potentially faulty results, (2) it offers a list of objects that are interesting per se and worthy of further as well as individual consideration, and (3) it will eventually allow for a population study of those types of objects. The large (and continuously growing) number of spectra recorded by the RAVE survey makes it impossible to evaluate all of them by hand. The identification of peculiar and SB2 spectra has to be carried out by automated procedures. To gain specific experience and to provide a comparison ground for the results of the automated procedure, we have nevertheless performed an eye inspection on each of the ∼25,000 spectra included in the second RAVE data release.

For the purpose of identification of peculiar and SB2 spectra, we have adopted a method based on the properties of the CCF between the observed spectrum $o(\lambda)$ and a synthetic template spectrum $t(\lambda)$,

$$\int_R o(\lambda) t(\bar{\lambda} - \lambda) d\lambda, \quad (1)$$

with integration covering the whole spectral range R and the synthetic spectrum taken from the library of Munari et al. (2005), the same as adopted for the main RAVE χ^2 analysis pipeline. The procedure works by examining several properties of the observed spectra and the CCF in a few steps. As an input it requires a flux-normalized observed spectrum, its S/N value, and a rough estimate of the effective temperature. The latter two values are already provided by the main RAVE analysis pipeline.

We have also tested other numerical methods that are commonly used for the purpose of classification—artificial neural networks, support vector machines, and principal component analysis. None of those methods worked well for our purposes, most likely due to the overwhelming number of different morphological features that are present in the observed spectra, which are extremely hard to efficiently represent in a training sample. For this reason we focused on the cross-correlation method, which is detailed in the following section.

2.1. Classification Procedure

The goal of the classification pipeline is to separate different types of spectra and to discover spectra with systematic or other observational errors. It is required that the value of the S/N is greater than 13. That limit was set in Z08 where it was shown that the estimation of atmospheric parameters for spectra at lower S/N becomes unreliable and only the major spectral lines are still distinguishable. It seems reasonable to assume that classification would also become unreliable below that limit.

Next, the minimal and maximal flux values are verified. If the minimal value (of any single pixel) is negative, the spectrum is rejected since it has clearly undergone some problems in background subtraction. On the other hand, the limits on maximal values are more problematic because rejecting spectra with emission lines is not our goal. Taking that into account, we set the upper limit to 1.5 by inspecting the normalized flux distribution of a large number of spectra. It showed that less than 1% of the spectra have their maximum flux above that value, mostly as a result of an artifact. Such spectra are not immediately excluded but are flagged as potential cosmic-ray hit candidates. Emission-line objects (see Figure 1(h)) are identified later.

In the next step, several properties of the CCF between the observed spectrum and the synthetic template are calculated and evaluated. The template spectrum is interpolated based on the library of synthetic spectra by Munari et al. (2005). We always construct the CCF using the same template. In our experience, this allows for an easier classification of unusual spectra (e.g., coronal emission, binaries, etc.) because in those cases the resulting CCF is not influenced by the erroneous formally best-matching normal star template, calculated by the parameter estimation pipeline. For the template, we use the average case of a dwarf with $T_{\rm eff} = 5800$ K, $\log(g) = 4.4$, and M/H = 0.0 (i.e., close to solar values). The calculation of the CCF is done with the same template for all observed spectra. This means that the peaks of CCFs of hotter stars, for example, will be weaker but it is of no concern since we are only interested in the particular shape of the CCF and not in its strength. For the same reason, the exact values of the selected atmospheric parameters of the template spectrum are not important and the properties of the CCF do not depend strongly on the values of those parameters. The observed spectrum is then re-binned to the template's wavelength range for an easier calculation. Z08 also showed that the projected rotational velocity ($v \sin i$) is not recoverable for a slowly rotating star, while the amount of α-enhancement ([α/Fe]) is unreliable and cannot be trusted for individual objects. Therefore, both parameters are set to zero. Another reason why a more careful selection of rotational velocity is not important is the fact that the width of the core of the CCF is much wider than the error of the typical rotational velocity estimate.

The wings of the CCF contain information about the oscillations of the spectral continuum. By comparing the asymptotic values of the wings, it is possible to eliminate all spectra that have uneven continuum and are unsuitable for modeling. Figure 1(b) shows a relatively high S/N spectrum with a strongly oscillating continuum. While the left wing converges to zero as it does in the case of a well-behaved single star spectrum, the right one does not. The difference of the two levels is a useful method for the detection of badly normalized spectra.

Distinguishing between different types of stellar objects (e.g., binary stars, emission stars, fast rotators) is harder than detecting spectra plagued by observational and systematic errors. Spectral features in the former might look similar in some cases (split

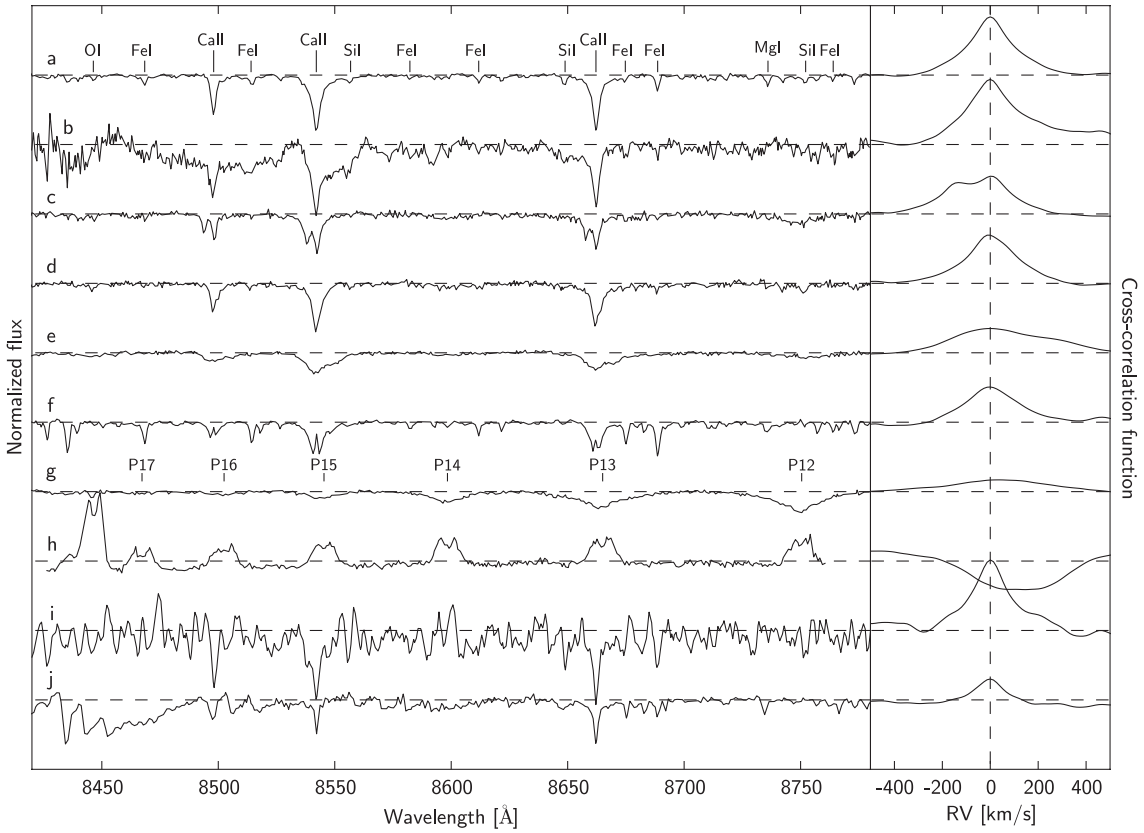

Figure 1. Spectra and CCFs of various stellar objects: (a) well-behaved spectrum of a G2V star, (b) spectrum with bad continuum fit, (c) wide SB2 binary candidate, (d) blended SB2 binary candidate, (e) W UMa type contact binary candidate, (f) star with chromospheric emission, (g) B5V star, (h) Be star, (i) carbon star, and (j) cold star with molecular bands (<3500 K). The dashed threshold lines are positioned at value 1 for spectra plots and at value 0 for CCF plots. All vertical scales are equal.

major lines in spectra of stars with chromospheric emission and double-lined binary spectra, for example). Counting the number of peaks of the CCFs is extremely efficient in the detection of potential SB2 binaries (Figure 1(c)). If the CCF has more than one central peak, the spectrum is clearly double-lined and probably comes from an SB2. In the case of blended SB2-like spectra, the CCF does not show two distinct peaks but is still asymmetric (Figure 1(d)). Unfortunately, CCFs of spectra of stars with chromospheric emission (Figure 1(f)) look similar to the previous case. Discriminating between those two classes is possible by measuring the width of the CCF and the level of asymmetry. The width of the CCF for a spectrum showing chromospheric emission cores is equal to that of the underlying star without the emission-line cores. The level of asymmetry is calculated by comparing the area under the left and right half of the CCF. It turns out that CCFs of blended binary candidates are wider and more asymmetric than those of stars with emission-line cores. The border values were set by inspecting a visually classified sample of both types. Stars with emission-line cores usually have stronger narrow metallic lines that help to distinguish between both types. In cases where spectral lines of an SB2 candidate are too blended, the detection of binarity is impossible. Further details on this topic are described in the following section.

Wide and shallow spectral lines are a signature of hot stars, where the otherwise dominant Ca II triplet is weak or absent and lines from the hydrogen Paschen series dominate. The CCF between such a spectrum and a template spectrum of a colder dwarf is wide and with low amplitude (Figure 1(g)). Since lines get wider and shallower with increasing temperature, it becomes increasingly difficult to recognize SB2 binary candidates among early A-type and hotter stars, even if they are observed at quadratures and close to edge-on inclinations. Fortunately, the fraction of hot stars among the high galactic latitude field RAVE stars is almost negligible. Relatively low amplitude and very wide CCFs are also observed in spectra of contact binaries. Most of the lines in such spectra display very little contrast with the underlying continuum: in addition to their intrinsic shallowness they are further widened by rapid rotation (Figure 1(e)). They too can be recognized by inspecting the asymmetry of the CCF. Fast rotating stars are another type of object that shows similar CCFs. According to Glebocki & Stawikowski (2000), the average projected rotational velocity becomes significant (greater than 30 km s^{-1} on average) for stars earlier than type F5, setting a limit at $T_{\rm eff} = 6600$ K. If some wide-lined spectrum that does not have a clear two-peaked CCF has a temperature above this limit, it is considered to be a fast rotator rather than a blended binary.

Peculiar types of stars are harder to classify since spectral features of such objects span a wide range of appearances. CCFs of special cases (Figures 1(h)–(j)) all look different from normal single star spectra. All such peculiar objects were flagged and later eye-checked to avoid any misclassification. A detailed description of the classification procedure along with the computer code is available upon request from the authors.

3. SB2 DETECTION SIMULATION

In this section, we explore which parameters have the largest impact on the probability of detection of an SB2 or a peculiar

star spectrum in the RAVE spectra sample. We also determine the limits of parameter space beyond which their detection is no longer possible.

3.1. Synthetic Sample

It is desired that the synthetic sample mimics the observed one as closely as possible. We expect that metallicity ([M/H]) and barycentric radial velocity are both distributed the same way for binary stars as they are for single stars, with the latter values measured by Z08. The similarity between the metallicity distribution among single and binary stars is discussed by Latham (2003). Additionally, we expect that both components should have roughly the same chemical composition and are both of the same age.

Although in the RAVE survey the number of dwarfs and giants is roughly similar, we assumed that only main-sequence binary stars are likely to be double-lined. For binaries of intermediate masses, it is highly unlikely to find one consisting of two giant components. There are two reasons for this: (1) to reach the giant stage at the same time, two stars must be almost equally massive (to within 1%) and (2) the lifespan of a giant is much shorter than the lifespan of a dwarf. Combining both criteria makes the probability of finding a giant–giant SB2 very small. Additionally, the morphology of a spectrum of a giant star is similar to a spectrum of a dwarf star with similar effective temperature. So even if we would be dealing with an SB2 spectrum of two giants, the classification method should not have any trouble recognizing that.

As a starting point for constructing a synthetic binary spectrum we took a distribution of temperature, metallicity, and radial velocity for single star dwarfs where we only included spectra with S/N $>$ 20 and $\log(g) > 3.5$ from the observed sample of 222,563 stars (from the internal release not yet publicly available) that had been previously confirmed as normal single stars by the classification method. After drawing random picks for the first star's temperature $T_{\rm eff,1}$ and [M/H] from those distributions both values were randomly varied for typical errors of both measurements, $\sigma_T = 300$ K and $\sigma_{\rm [M/H]} = 0.2$. This was done in order to make both distributions smoother. Using the two values, we found a complete set of parameters (mass, radius, and I magnitude) for the first star from a Yonsai–Yale isochrone (Yi et al. 2001) of appropriate iron abundance and an age of 200 Myr. This particular age was chosen so that all stars are already settled on the main sequence and the hotter ones still did not have time to turn to giants, setting the corresponding upper mass cutoff at approximately 3 solar masses. The age dependence of the stellar parameters for the stars on the main sequence can be neglected and the selection of the age of the isochrone is not very important. Similarly, we also neglected the minor effect of α-enhancement and its value was kept fixed at zero during the calculation of all spectra. This provides us with all the necessary parameters for the construction of the synthetic spectrum of the first component. Now we randomly select a luminosity ratio η, which is defined as

$$\eta = 10^{\frac{2}{5}(I_1 - I_2)}, \quad (2)$$

where I_1 and I_2 are the brighter star's and the fainter star's I magnitudes, respectively. This ratio is selected from an interval of [0, 1]. From there on it is straightforward to find the position on the same isochrone with a matching I magnitude of the second component. Distributions of stellar masses, radii, mass ratios, and luminosity ratios in the final sample are shown in Figure 2.

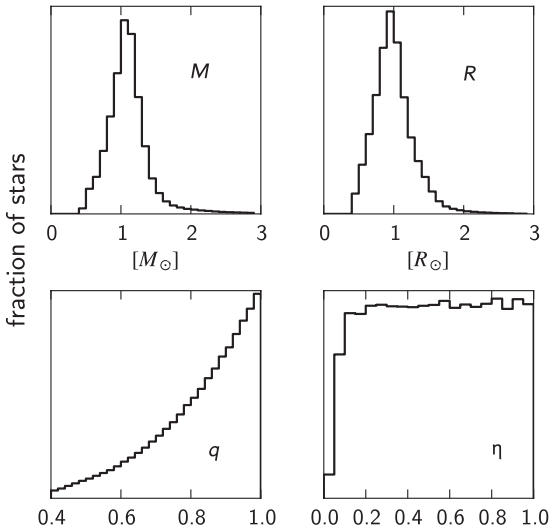

Figure 2. Distributions of stellar masses (M), radii (R), mass ratios (q), and luminosity ratios (η) of synthetic binary stars. The distribution of luminosity ratios is flat except for very small values where the systems could not be modeled because of the consequently large temperature difference.

The orbital period was chosen randomly from a distribution fitted to observations in Duquennoy & Mayor (1991),

$$f(\log P) = \frac{dN}{d\log P} = C \exp\left\{\frac{-(\log P - \overline{\log P})^2}{2\sigma^2_{\log P}}\right\}, \quad (3)$$

where $\overline{\log P} = 4.8$ and $\sigma_{\log P} = 2.3$ and P is in days. A similar distribution was also found in numerical simulations of star cluster evolution by Bate (2009). A limit on the short period was selected at 0.2 day, because the period distribution for eclipsing binary stars in Malkov et al. (2006) shows a strong cutoff there. On the longer end, we took a generous limit of two years. At such long orbital periods, the orbital velocities become so small that the fraction of detectable binaries becomes negligible. For a binary system of two solar twins on a circular orbit, the maximal velocity amplitude is equal to 30 km s^{-1} for a period of two years. Knowing the orbital period, the semimajor axis and orbital velocities were calculated using Kepler's third law. We assumed that all systems have circular orbits. This only holds true for very short period systems ($P < 10$ days). The eccentricity of systems with $P < 500$ days can be significant with a mean of about 0.3, according to Duquennoy & Mayor (1991). Nevertheless, the differences of orbital velocities of such systems compared to the velocities of similar systems with circular orbits are small in most cases, justifying the upper assumption. The orbital phase and orbital inclination to the line of sight were selected randomly.

The rotational velocities of both stars were calculated by assuming that the stars co-rotate with the system's orbital rotation. The minimal rotational velocity was set at 20 km s^{-1}, similar to the value typically obtained by RAVE's parameter estimation pipeline for slowly rotating single stars. While this value is unrealistically high, it simulates the marginally lower resolving power of the observed spectra compared to the synthetic ones, where the difference is easily compensated for by slightly wider lines of faster rotators. Some of the close binary systems were removed from the simulation since their rotational velocity exceeded the highest velocity supported by the spectra library from Munari et al. (2005). The overall number of such

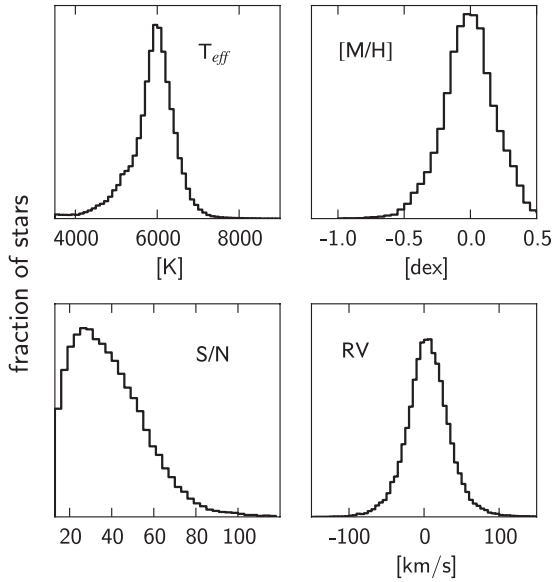

Figure 3. Observed distributions for temperature, metallicity, S/N, and barycentric radial velocity for single stars from which the simulated parameters for synthetic binaries are drawn.

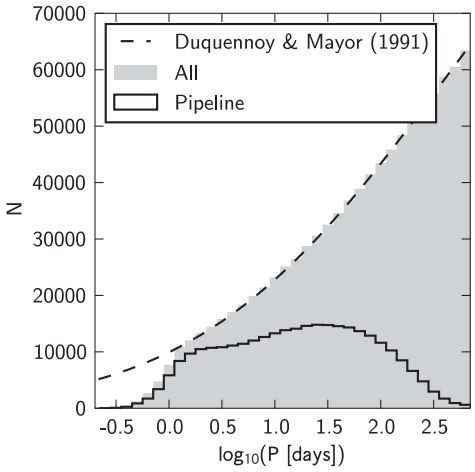

Figure 4. Initial distribution of orbital periods and the distribution of periods of detected systems. The dashed line shows the predicted distribution from the literature given in Equation (3). The shaded gray histogram shows the actual initial distribution of the simulation without the systems with very short periods. The black solid histogram shows the number of detected systems in the simulation.

systems is very small and their omission should not affect the end results of the simulation.

Synthetic spectra were then scaled according to the luminosity ratio η, Doppler-shifted to their projected orbital velocities, summed and normalized, and finally, the barycentric radial velocity drawn from the distribution shown in Figure 3 was applied. To simulate the observational errors, Gaussian noise was added to the binary spectrum according to the randomly selected value of S/N from the distribution also shown in Figure 3. Errors in the normalization of the continuum were simulated by introducing five cosine functions with random phases, frequencies, and amplitudes matching typical variations in observed spectra. We generated 10^6 such binary spectra that were then classified with the method described in the previous section.

3.2. Simulation Results

One of the results yielded by the simulations is the distribution of system periods at which the binarity is detectable. The limitations on the short- and long-period ends come from two different factors. The spectral lines of short-period binaries are widened because of the co-rotation of both components. Another reason for the widening is velocity smearing during the exposure which becomes significant only for the systems with the shortest periods ($P < 1$ day). Combining both effects can blend the lines of even a relatively well-separated system, making detection more difficult. On the long-period end, the detection probability is affected by the limited resolving power of the spectrograph and the fact that binarity detection strongly depends on the noticeable double peaks of the relatively wide Ca II triplet lines. For example, a binary system of solar twins orbiting around each other on a circular orbit with a period of one year and seen along a line of sight close to orbital plane is just on the threshold of detection when observed at a quarter phase.

Figure 4 compares the distribution of the input binary systems and those recovered by our analysis. The dashed lines show the distribution of periods given in Equation (3), while the shaded gray histogram shows the input period distribution. The systems with the shortest periods are missing partly because it was not possible to model spectra of fast rotating cool stars and partly because we removed all systems that exhibited Roche overflow, i.e., in which the stellar radii became greater than the radius of the Roche lobe R_L given by Eggleton (1983),

$$\frac{R_L}{a} \approx \frac{0.49q^{2/3}}{0.6q^{2/3} + \ln(1 + q^{1/3})}, \quad (4)$$

where a denotes the semimajor axis and q denotes the mass ratio. The solid line in Figure 4 shows the number of systems that were confirmed as binaries by our classification method. The number of modeled systems is small below $P \leqslant 1$ day and predictions there should not be trusted. The detection ratio becomes very high for systems with periods between 1 and 10 days. For systems with periods between 10 and 100 days, the detection rate is still significant. For $P \geqslant 100$ days the number of recovered binaries rapidly drops, becoming negligible at 1 yr.

The dependence of the ratio between the number of properly classified and all binary systems (detection ratio) on various parameters is shown in Figure 5. For all synthetic spectra the classification was done at only one orbital phase, i.e., for a "single shot." A tight relation between mass ratio q and luminosity ratio η comes from the fact that only main-sequence stars were included in the simulation sample. More interestingly, both S/N diagrams (q–S/N and S/N–η) show that the detection is almost independent of the S/N as long as $\eta \gtrsim 0.3$ or equivalently $q \gtrsim 0.75$. The detection ratio is equal to the simulation average of ~31%. A slightly worse detection is observed at S/N < 20, while the seemingly lower detection ratio at S/N > 80 is a consequence of the small number of such systems in the simulation.

The detection clearly depends strongly on the system period P and the difference between the projections of the orbital velocities of stars $\Delta v_{\rm orb}$. The detection ratio is higher than 80% for 0.8 days $< P <$ 2 days as long as $\eta \gtrsim 0.3$. It seems that it begins to decrease at shorter periods but this again comes from the fact that very few systems were modeled in this region. For $P < 30$ days, the detection is still better than 50% and falls toward 0 at roughly 1 yr. The unexpectedly high yield of binaries at short periods and $\eta < 0.3$ can be explained as the

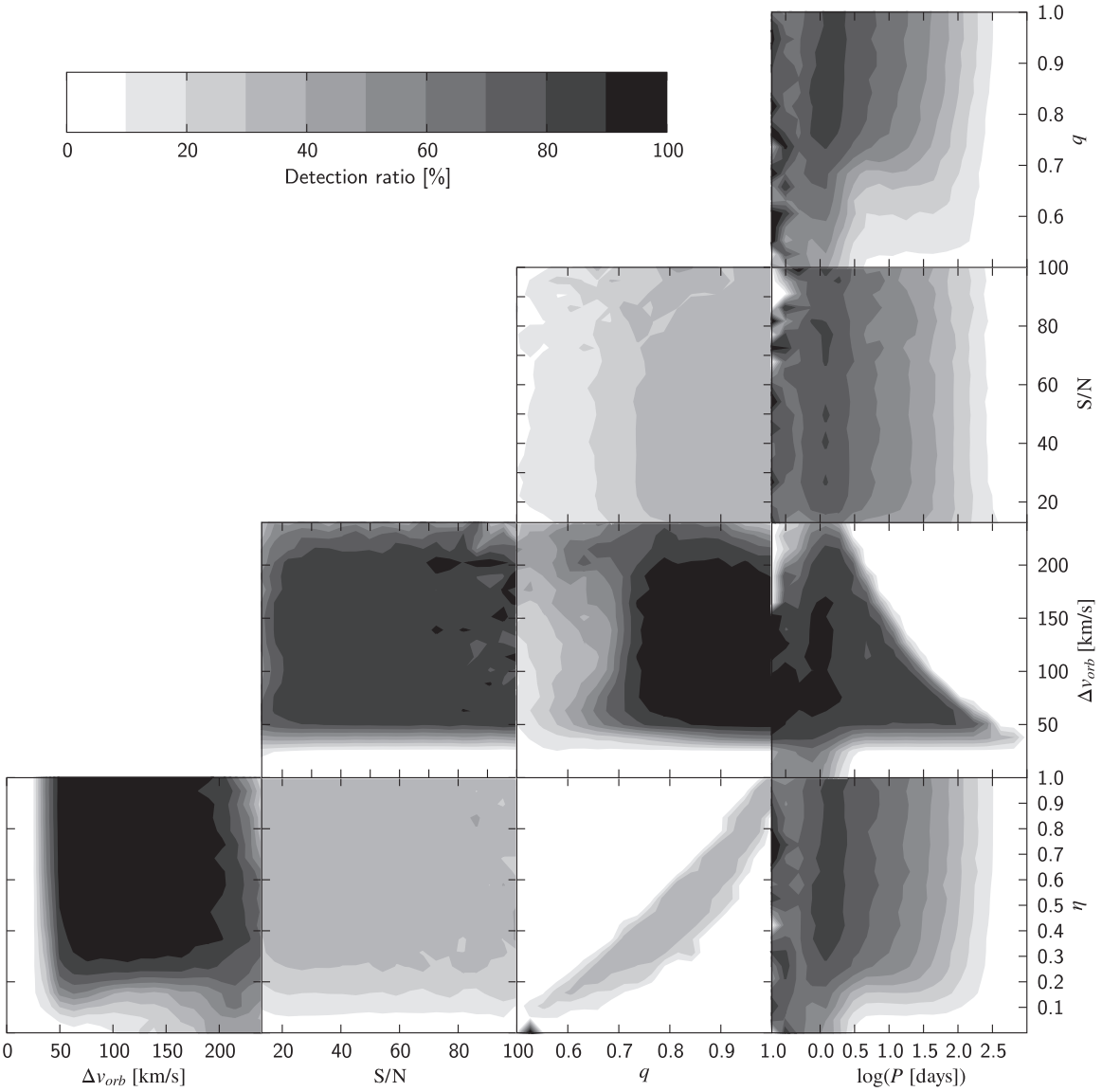

Figure 5. Ratio between detected systems and all systems in a given surface element as a function of the parameters $\Delta v_{\rm orb}$, S/N, q, log P, and η.

result of the incorrect classification of rapidly rotating cool stars as blended binaries.

The same properties can be seen on the diagrams that show the dependence of the detection ratio on the velocity difference. At $\Delta v_{\rm orb} > 40$–50 km s^{-1}, the probability of detection is greater than 90% as long as $\eta \gtrsim 0.3$. Observed spectra sometimes have a slightly lower resolving power than the model ones because of non-optimal focusing. Taking that into account it is safe to take 50 km s^{-1} as a lower limit. Below that value the probability for detection quickly vanishes.

The simulation shows that the target population consists mostly of binary systems with relatively well-separated spectral lines ($\Delta v_{\rm orb} > 50$ km s^{-1}) and mass ratios close to unity ($q > 0.75$). Consequently, this implies that only shorter period binaries with $P < 1$ yr will be detected, independent of the S/N, and additionally justifies the circular orbit assumption.

Since the orbital period is not measurable from a single observation, it is convenient to plot the distribution of orbital periods for all systems with a given $\Delta v_{\rm orb}$ (shown in Figure 6). The range of orbital periods at lower velocities is greater than at higher velocities, meaning that it is possible to guess the system's period more precisely for binaries with better separated lines.

The fraction of SB2 binaries that are classified as normal single stars in the observed sample is of minor concern for studies of Galactic structure. Mistakenly treating a blended SB2 spectrum as a single one does not yield extremely wrong results because the centroid of the blended correlation peaks should be close to the systemic velocity. As for the atmospheric parameters, the similarity of both components ensures that the single star spectrum fit will still be some average of both spectra and will thus not be far from the proper solution for each component. Usually, only the rotation velocity is overestimated, but this parameter is not measurable from RAVE spectra with noteworthy precision anyway.

4. BINARY STAR LIST

We ran our automated classification method on the 23,321 stars in the RAVE second data release (Z08) with computed atmospheric parameters and an S/N > 13. A total of 467 spectra was labeled as SB2 candidates. Upon checking all of

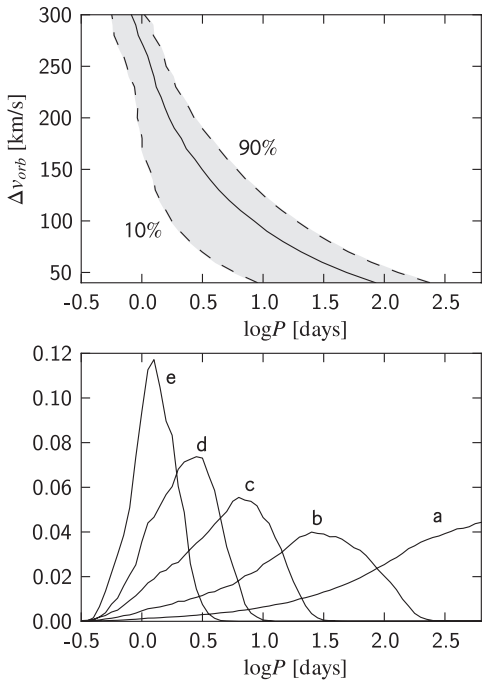

Figure 6. Shaded region in the top diagram shows the area between the 10th and 90th percentile of a distribution of line separations as a function of log P. For example, at 200 km s^{-1} the majority of spectra (80%) are from systems with orbital periods between 1 and 3 days. The solid line is the distribution median. The bottom diagram shows the distribution of orbital periods of systems with different line separations (a: 0–50 km s^{-1}; b: 50–100 km s^{-1}; c: 100–150 km s^{-1}; d: 150–200 km s^{-1}; e: $>$ 200 km s^{-1}) as a function of log P.

them manually, only 129 of them (belonging to 123 different stars) could undoubtedly be confirmed as SB2 candidates, implying a success rate of 0.3. For 102 of these 129 spectra, the automated classification was able to measure the separation in radial velocity, the individual temperatures, and the luminosity ratio. These data are summarized in Table 1. The first six columns of the table report the star and spectrum identification as given in the RAVE second data release (accessible through http://www.rave-survey.org), S/N is the spectrum signal-to-noise ratio, $\Delta v_{\rm orb}$ is the difference between red and blue Doppler-shifted lines, $\Delta v_{\rm orb}$ error is an error of that estimate, and η is the luminosity ratio of the less luminous to the more luminous component. $T_{\rm eff,1}$ and $T_{\rm eff,2}$ are blueshifted and redshifted component's effective temperatures, respectively. The 27 spectra for which the automated procedure could not reliably derive the separation in orbital velocity, the luminosity ratio, and temperatures of the two stars are given in Table 2.

All 22,854 spectra classified as "normal single stars" by the automated procedure were checked manually one by one, and none of them appeared to be an undetected SB2 candidate. We can conclude that the automated procedure has been successfully detecting essentially all genuine SB2 candidate spectra present in the RAVE second data release. The extra spectra picked out by the automated procedure are spurious detections caused by cool stars with wider than usual absorption lines.

The preliminary eye-inspection check carried out on the sample of RAVE second data release flagged 107 stars as potential SB2 objects. Our automatic classifications confirmed 71 of them. The remaining 36 spectra could not be confirmed even after thorough inspection and were therefore discarded.

4.1. Binary Spectra Fitting

The stellar parameters and radial velocities were obtained by fitting the observed binary spectra with the synthetic spectra from the library. While many methods exist for fitting single star spectra (see, e.g., Koleva et al. 2009, and references therein), none of them was reportedly used on SB2 spectra. Modeling binary spectra is more complex than modeling single star spectra for obvious reasons. The number of free parameters is more than twice as large. In our case, where we neglected all minor effects, the total number of parameters was 10: effective temperatures of both stars, their surface gravities, rotational velocities, metallicity, which was assumed to be the same for both stars, both Doppler shifts, and the luminosity ratio.

The common way of finding the best-fitting solution is to define a criterion for the goodness of fit, which is usually the sum of squares of the difference between the observed (o) and modeled (m) spectra, where the sum goes through all wavelength bins.

Our fitting procedure works as follows. First, the approximate Doppler shifts and luminosity ratio are obtained with the TODCOR method (Zucker & Mazeh 1994). The parameters of both template spectra for the calculation of the CCF are always the same. With roughly known velocities and luminosity ratio, a better solution is searched for using a MultiNest algorithm (Feroz et al. 2009). This method has two big advantages over more traditional algorithms like the Nelder–Mead simplex. The final solution of the latter depends on the initial starting point on the grid of synthetic spectra. Moreover, because we are using a linear interpolation of synthetic spectra between the grid points, descending methods have a bias for finding a solution close to some grid point. Parameter space sampling methods on the other hand have a better feel for the area surrounding the global minimum and therefore a better chance of finding it.

Unfortunately, none of the tested methods gave reasonable results in performing a completely unconstrained fitting. It often happened that the method returned a solution consisting of a giant and a dwarf both with similar temperatures and a luminosity ratio close to unity. While this solution might formally be the best-fitting one, it is still not physically feasible and cannot be trusted. To overcome the problem we limited the solutions to the main-sequence stars, the same as we did in the construction of the synthetic sample for the described simulation (see Section 3.1). This simplification gave more reasonable solutions (Table 1).

The errors of the $\Delta v_{\rm orb}$ are similar to the errors of measured radial velocities for single stars. Generally, they are larger for blended cases, where positions of lines are harder to locate and for faster rotating stars that have wider lines. Errors on individual spectral types and luminosity ratio were estimated from four re-observations. The objects T_9474_01354_1, T_8045_00353_1, T_8510_01121_1, and T_4916_01130_1 were all observed twice on different nights. The average effective temperature difference between the two solutions for the same object is equal to 130 K with a standard deviation of 44 K, similar to what is returned by the MultiNest method. The errors depend on the S/N and the separation of the lines (Doppler shifts). They are greater when the lines are closer together. The average difference of the luminosity ratio is equal to 0.08 with a standard deviation of 0.08. Here, the dependence on line separation is much greater. When lines are separated well ($\Delta v_{\rm orb} \gtrsim 100$ km s^{-1} for both measurements) the errors are smaller than 5%, but are proportionally higher in the blended case of T_9474_01354_1

Table 1
SB2 Candidate Spectra with Solutions

ID	R.A. (°)	Decl. (°)	Obs. Date	Field Name	FNum	S/N	$\Delta v_{\rm orb}$ (km s^{-1})	$\Delta v_{\rm orb}$ error (km s^{-1})	η	$T_{\rm eff,1}/T_{\rm eff,2}$ (K)
T8022_00693_1	0.39312	−45.92950	20040825	0004m46	80	42	83.5	4.6	0.65	6500/6200
T7527_00046_1	3.53638	−41.86767	20041022	0010m40	135	69	89.2	4.2	0.39	6600/5800
T8472_01036_1	9.15758	−59.53453	20041122	0049m60	49	46	170.9	3.8	0.80	6000/6200
T8035_00549_1	18.67075	−48.29000	20040824	0110m48	107	41	57.6	8.9	0.65	5700/6000
T8039_01118_1	20.92058	−50.02906	20040824	0110m48	132	43	131.3	3.2	0.64	6600/6300
T8480_00202_1	21.03983	−59.11883	20040827	0133m59	40	66	61.2	6.5	0.79	6200/6000
C0136059-154303	24.02483	−15.71775	20041022	0136m15	132	40	81.6	7.8	0.84	5800/5600
T8045_00353_1*	30.10787	−49.07056	20041030	0213m49	43	32	153.6	4.7	0.67	6600/7000
T8045_00353_1*	30.10787	−49.07056	20041223	0213m49	43	45	136.0	4.5	0.63	6900/6500
T8045_00967_1*	32.36425	−49.55372	20041223	0213m49	35	35	118.0	4.9	0.55	5600/6100
T7554_01089_1	33.70387	−41.39386	20041122	0206m42	98	71	68.2	4.6	0.95	6200/6200
T8489_00816_1	34.45954	−58.06731	20041025	0212m56	132	52	92.0	4.9	0.47	6000/5400
T8055_01000_1	35.35021	−50.69675	20041223	0213m49	132	63	126.5	3.4	0.78	6100/6300
T4704_00341_1	38.18088	−5.46006	20041202	0238m05	50	76	95.6	3.0	0.95	5900/5900
T9155_00658_1	48.67517	−71.48606	20041231	0320m73	74	48	80.2	6.0	0.27	5400/6400
T9155_01488_1[a]	50.74250	−70.78867	20041122	0320m73	76	35	228.4	4.8	0.62	7000/6600
T8493_00812_1	50.80117	−52.66894	20041221	0329m52	50	71	62.2	10.6	0.57	6000/6400
T8867_00392_1	52.61408	−60.71822	20041222	0336m62	68	47	94.0	4.3	0.95	6200/6100
T8063_00152_1	53.43492	−47.79075	20040924	0342m46	28	52	103.3	5.6	0.82	6400/6500
T8060_01804_1	54.98733	−47.20036	20040924	0342m46	18	54	99.4	6.1	0.56	6400/5900
T8867_00641_1	56.42312	−60.73789	20041222	0336m62	89	59	114.3	3.5	0.86	5800/5700
C0405287-664250	61.36975	−66.71392	20041229	0403m68	78	34	154.4	4.9	0.61	6100/5700
T8510_00159_1	71.55858	−53.18144	20041122	0447m52	52	43	93.5	6.0	0.47	5600/6200
T8510_01121_1*	73.24871	−53.44589	20041122	0447m52	132	43	116.1	3.4	0.92	6200/6300
T8510_01121_1*	73.24871	−53.44589	20041123	0447m52	132	70	83.8	3.3	0.92	6100/6200
C0454137-482550	73.55742	−48.43067	20041129	0449m46	143	19	138.5	5.5	1.00	5800/5800
T6469_01030_1	74.22913	−26.67475	20041023	0504m26	29	81	150.9	4.9	0.97	7500/7500
T8077_00505_1	74.23212	−45.94442	20041129	0449m46	97	38	72.2	6.5	0.32	6400/5500
T7053_00933_1	77.98013	−36.82828	20050129	0516m37	61	43	144.6	3.8	0.41	6200/5500
T7594_00902_1	79.94879	−42.58228	20041025	0520m42	18	54	121.6	6.3	0.22	5200/6400
T6501_00207_1	84.38304	−29.27319	20050128	0535m29	94	29	110.9	4.3	0.42	5700/6400
C0538506-401127	84.71121	−40.19092	20050221	0549m40	46	34	125.5	5.3	0.67	6100/5700
T9386_01431_1	84.90012	−79.97753	20050128	0609m80	40	40	251.4	6.4	0.42	7300/6400
T8891_03299_1	85.22208	−67.12572	20041222	0517m65	130	58	135.2	4.1	0.94	6800/6900
T9163_00869_1	88.10375	−68.15956	20041229	0614m68	45	32	73.1	7.7	0.79	5400/5600
T7606_01468_1	88.90250	−42.68181	20041129	0549m40	143	55	122.3	6.2	0.23	6500/5300
T8894_00627_1	95.01929	−60.68039	20041122	0611m63	84	41	140.4	3.4	0.98	6500/6400
T8898_00763_1	97.86787	−63.53539	20050129	0611m63	120	56	169.2	6.5	0.32	6300/7600
OCL00153_1457872	114.89513	−16.35411	20041202	0739m14	143	37	97.5	5.2	0.22	6600/5400
T5491_00836_1	156.59321	−8.73600	20040510	1025m08	118	62	166.1	4.4	0.57	6400/6000
C1040349-123408	160.14554	−12.56892	20050221	1042m11	32	19	124.4	7.0	0.53	6000/5500
T4916_01130_1*	160.17733	−4.73567	20041231	1040m04	136	59	136.6	3.9	0.54	5300/5800
T4916_01130_1*	160.17733	−4.73567	20050131	1040m04	136	52	141.1	4.3	0.49	5600/5100
T0255_00172_1	163.44150	0.70903	20050331	1101m01	59	67	165.0	4.3	0.52	6500/6000
T6076_01000_1	163.57917	−17.06961	20050301	1101m15	19	64	64.9	7.4	0.90	5700/5800
T6661_01196_1	169.15446	−29.64906	20040628	1114m29	107	68	56.1	7.7	0.70	5900/5600
C1153324-145540	178.38538	−14.92797	20040508	1200m15	49	20	82.7	5.5	0.85	6400/6300
C1154492-321905	178.70504	−32.31819	20050130	1204m33	53	22	75.8	5.3	0.57	5200/5600
T7235_00510_1[b]	180.36558	−32.22625	20050130	1204m33	65	43	150.5	4.6	0.82	6200/6000
T5519_01279_1	181.30896	−9.36233	20040704	1200m09	117	79	161.8	4.5	0.29	7600/6500
T7245_00609_1	185.15921	−35.80486	20040628	1232m34	23	29	131.0	4.8	0.89	6400/6500
T6690_01250_1	187.25942	−26.25542	20050226	1226m28	81	72	156.9	5.0	0.88	6600/6500
C1239461-315947	189.94237	−31.99644	20040628	1232m34	89	36	151.5	8.8	0.42	6100/5400
T6709_00114_1	193.29750	−29.43997	20040704	1252m28	123	77	51.7	6.6	0.99	6100/6100
C1300428-055402	195.17838	−5.90081	20040629	1252m05	115	20	110.1	4.4	0.97	5100/5200
T6717_00250_1	201.29679	−24.86047	20050221	1321m22	146	58	61.9	7.3	0.64	6100/5700
T7270_00030_1	206.95521	−33.42233	20040627	1353m32	17	78	133.7	4.0	0.92	7200/7400
T6148_00058_1	208.41325	−21.83800	20050301	1345m21	120	70	74.2	5.3	0.98	5500/5500
T6148_00150_1	208.46092	−22.48617	20040529	1345m21	129	70	154.8	3.4	0.71	6200/6500
T6142_00026_1	212.89283	−17.22064	20040705	1408m19	81	40	59.5	10.4	0.41	5300/6000
T7282_00604_1	214.94333	−30.97186	20040507	1419m30	12	64	123.5	5.8	0.40	6000/6800
T4999_01159_1	224.55354	−6.32244	20050320	1456m05	90	97	168.4	6.4	0.34	6400/7800
C1514052-223119	228.52179	−22.52217	20050321	1524m21	32	18	188.2	7.9	0.92	6600/6700
154550	257.02162	−41.25581	20040924	1716m42	60	70	83.5	3.2	0.70	6100/5900
TYC_6269-14-1	274.46946	−17.31033	20040925	1822m16	15	47	106.9	6.2	0.43	9400/7500

Table 1
(Continued)

ID	R.A. (°)	Decl. (°)	Obs. Date	Field Name	FNum	S/N	$\Delta v_{\rm orb}$ (km s^{-1})	$\Delta v_{\rm orb}$ error (km s^{-1})	η	$T_{\rm eff,1}/T_{\rm eff,2}$ (K)
T9458_00473_1	285.11504	−76.27161	20040825	1929m76	43	98	150.0	3.1	0.48	6900/6300
T9458_00642_1	289.45371	−75.53994	20040502	1929m76	61	53	88.3	4.9	0.49	6800/6200
C2002522-265300	300.71754	−26.88344	20040530	2008m28	66	36	95.2	4.7	0.29	6000/5000
T6327_00704_1	302.40129	−21.45864	20040530	2016m23	64	72	210.8	9.8	0.80	8500/8000
T8776_00144_1	303.03658	−52.97231	20040825	2018m53	50	46	88.4	4.2	0.83	5700/5900
T6340_00410_1	305.15842	−22.04008	20040529	2016m23	83	38	71.5	5.0	0.43	5600/6300
T6333_00993_1	306.12083	−16.89067	20040529	2024m18	68	51	104.3	4.3	0.28	7600/6200
T5766_01122_1	306.83275	−14.16467	20040629	2034m12	22	50	147.8	4.6	0.89	6000/6100
T9308_00697_1	307.64242	−68.24917	20040902	2037m70	71	35	85.2	8.5	0.83	5300/5500
C2033361-142800	308.40050	−14.46683	20040531	2034m12	4	24	101.2	6.0	0.34	6000/5200
T6330_00204_1	308.44429	−16.76408	20040531	2024m18	98	34	69.7	5.8	0.45	6300/5700
T7468_01360_1	308.69225	−36.47119	20040508	2028m35	134	63	73.7	6.5	0.35	6600/5800
T9316_00774_1	308.77992	−71.66714	20040629	2037m70	144	40	245.5	4.0	0.83	7400/7100
T9312_00707_1	309.10854	−70.08231	20040629	2037m70	102	39	71.3	4.6	0.81	6100/6200
T7468_00041_1	309.32412	−36.77611	20040706	2028m35	131	27	67.1	10.6	0.41	6400/5900
T9329_00060_1	313.35037	−71.83719	20040902	2037m70	131	71	73.3	5.8	0.68	6300/6000
T6345_01096_1	315.91971	−15.25700	20040627	2058m13	136	92	89.3	3.6	0.58	5900/6300
C2122581-243821	320.74225	−24.63917	20040531	2133m24	41	21	150.4	4.2	0.64	5700/5400
T8806_00524_1	321.79408	−54.34042	20040924	2136m53	38	45	178.3	4.8	0.54	5700/5200
T9474_01354_1*	322.07942	−75.95464	20041003	2106m75	114	39	85.1	4.1	0.72	5600/5300
T9474_01354_1*	322.07942	−75.95464	20041025	2106m75	114	48	62.6	9.4	0.50	5100/5600
C2142493-091026	325.70562	−9.17411	20040628	2133m08	117	22	78.6	4.2	0.90	5500/5600
T8812_00684_1	326.68233	−55.19394	20040924	2136m53	134	36	116.8	4.3	0.69	6600/6300
T7495_00875_1	330.05267	−35.33600	20040607	2153m35	115	30	119.4	5.2	0.74	5400/5200
T7495_01110_1	331.44988	−35.75942	20040607	2153m35	117	59	118.4	3.2	0.76	5600/5400
T5810_00770_1	335.97663	−13.81914	20040628	2216m13	114	66	86.0	3.0	0.56	6500/6100
T7498_00637_1	339.87038	−31.50889	20040825	2247m33	60	43	87.6	5.2	0.70	6200/6000
C2240261-515558	340.10892	−51.93294	20040827	2258m52	43	34	114.0	4.8	0.46	5400/6000
T8450_00444_1	341.65946	−48.38072	20040824	2239m47	117	90	51.3	6.7	0.69	6400/6200
T8824_01026_1	344.63675	−54.00822	20040827	2258m52	149	46	146.7	3.6	0.83	5800/5600
T5827_00145_1	348.04021	−13.04881	20040627	2314m11	21	82	140.6	3.4	0.89	6100/6000
C2317138-020625	349.30762	−2.10719	20040626	2313m03	86	28	131.7	5.7	0.63	5900/5600
T6399_00230_1	350.09596	−19.02089	20041031	2321m20	67	32	82.8	3.9	0.99	5500/5500
C2348525-211646	357.21913	−21.27961	20041101	2342m23	87	20	92.8	8.2	0.46	5800/6400
T9127_00460_1	358.00408	−60.74483	20040824	0004m59	17	46	72.4	6.6	0.51	6400/6000
C2352470-522138	358.19604	−52.36069	20041025	2351m52	62	29	86.8	6.9	0.49	5800/6400
C2353295-442121	358.37329	−44.35589	20041030	2339m43	126	18	102.7	7.1	0.39	5200/6000

Notes. Spectra IDs marked with asterisks were observed twice. The second observation of object T8045_00967_1 is listed in Table 2.
[a] A known binary star, Heintz (1992).
[b] DZ Hya, eclipsing binary of the Algol type.

(more than 20%). This holds true only if the main-sequence assumptions can be justified.

4.2. Notes on Individual Objects

While the spectra listed in Table 1 do not show any special features, some of those in Table 2 do and can be grouped together.

4.2.1. Ca II Emission

Six different objects (one observed twice) show chromospheric emission in the Ca II lines, similarly to what is sometimes observed in the same lines of single stars. All iron lines, especially the ones at 8515 Å, 8647 Å, and 8688 Å, show duplicity (Figure 7), although they are harder to identify in some of the noisier spectra. All seven spectra are consistent with G-type stars. The Ca II triplet lines of both components are too shallow, which indicates that some of the flux originates from emission processes. These stars are probably members of the RS CVn group of binaries with active chromospheres. G spectral types and emission cores in the Ca II lines are their distinctive features, with the active chromospheres powered by intense magnetic fields generated by tidal interaction between the two components (Foing et al. 1989; Eker et al. 2008). Object T5844_00340_1 was observed twice in the span of one month and shows changes in the positions of lines. Iron lines in C0232159_055451 are hardly observable, but shapes of the Ca II triplet lines are consistent with other objects of this kind.

4.2.2. Contact Binaries

Another group of morphologically similar spectra are potential new contact binary stars, shown in the middle plot of Figure 7. Four of the stars, BE Scl, DX Tuc, V1054 Cen, and DY Cet, are known W UMa type eclipsing binaries. Fifth, IV Pav, is still listed as an RR Lyr type variable in the SIMBAD database, but it was already suggested from *Hipparcos* observations that it might be a close binary (Solano et al. 1997; Fernley et al. 1998). Consistent shapes of spectra with very wide Ca II lines that are still clearly separable indicate a small semimajor axis and co-rotation of both stars. The other seven spectra in

Table 2
Peculiar and Low S/N SB2 Candidate Spectra

ID	R.A. (°)	Decl. (°)	Obs. Date	Field Name	FNum	S/N	Comment
T5844_00340_1*	1.20621	−21.69836	20040923	0014m21	35	37	Ca II emission
T5844_00340_1*	1.20621	−21.69836	20041024	0014m21	34	33	Ca II emission
C0028572-081237	7.23858	−8.21047	20040629	0030m06	2	24	Contact?
TC0102115-380905	15.54792	−38.15161	20040924	0103m37	8	29	Contact?
C0102282-105314	15.61779	−10.88733	20041202	0053m11	109	19	Low S/N
T5275_00027_1	15.86400	−12.17308	20041202	0053m11	124	83	Contact?
T6427_00323_1	20.38729	−29.13131	20040825	0111m27	132	64	BE Scl, W UMa type
T5855_00622_1	25.11900	−16.10931	20041023	0136m15	134	63	Ca II emission
T8045_00967_1*	32.36425	−49.55372	20041030	0213m49	35	15	Low S/N
C0232159-055451	38.06658	−5.91428	20041202	0238m05	44	24	Ca II emission
T5291_00361_1	39.63825	−14.29908	20040902	0231m12	131	99	DY Cet, W UMa type
C0238506-130910	39.71104	−13.15300	20040902	0231m12	116	34	Ca II emission
C0241430-062149	40.42942	−6.36364	20041202	0238m05	123	32	Contact?
T8093_00960_1	79.82367	−49.64683	20041101	0523m48	22	16	Low S/N
T8905_00616_1	91.98046	−66.36028	20041221	0614m68	72	77	Contact?
T7216_00384_1	174.61763	−30.29139	20040627	1138m31	74	74	HD 101167, triple
C1230542-330934	187.72588	−33.15950	20040531	1232m34	53	25	Low S/N
T6103_01209_1	188.19242	−16.43886	20040706	1223m16	110	63	Contact?
T7246_01161_1	188.20421	−35.69497	20040531	1232m34	143	47	V1054 Cen, W UMa type
C1245296-302913*	191.37354	−30.48700	20040529	1252m28	15	24	Low S/N
C1248186-101332	192.07758	−10.22578	20050322	1246m11	82	29	Ca II emission
T6130_00031_1	205.69717	−18.88536	20050301	1345m21	72	73	Contact?
O00337_2343045	207.45533	−62.23206	20040728	1352m62	80	47	Corrupted wavelengths
T6159_00232_1	223.16154	−18.37425	20040501	1452m20	76	69	Ca II emission
T9316_00114_1	308.68708	−72.61533	20040902	2037m70	4	48	IV Pav, RRLyr type, contact?
C2256145-342140	344.06067	−34.36114	20040825	2247m33	129	16	Low S/N
T9130_01530_1	359.33967	−64.24322	20040902	0009m65	60	67	DX Tuc, W UMa type

Notes. The wavelength calibration of the spectrum of O00337_2343045 is wrong, but it can nevertheless still be unambiguously confirmed as an SB2 candidate. The second observation of C1245296_302913 is not listed since its spectrum could not be recognized as a potential SB2.

the diagram are very similar to those of known contact binary spectra. It is likely that all of them are close binary systems.

4.2.3. HD 101167

The spectrum of HD 101167 is particularly interesting since it shows three components (bottom plot in Figure 7). Three Ca II lines as well as the 8674 Å Fe I and 8442 Å O I lines are clearly triple. The best-fitting solution suggests that the system consists of two early-type G stars at roughly ± 100 km s^{-1} and one late-type G star at ~ 0 km s^{-1}. A proposed explanation is a hierarchically ordered triple system with a fainter and cooler star orbiting around the center of mass of a closer system of two hotter components. HD 101167 is extraordinarily similar to the triple G-type system CN Lyn, already studied over the RAVE wavelength range by Munari (2003).

5. DISCUSSION AND CONCLUSION

This paper presents a method to identify SB2 candidate spectra among a sample of stellar spectra covering the near-IR Ca II triplet region at a resolution of $R \sim 7500$, and a list of discovered binaries in the latest RAVE data release. From repeated observations of the same objects it is also possible to detect SB1 spectra, which will be discussed in a forthcoming paper. Joining both types will give a basis for the population study of binary stars in the RAVE survey.

The classification method based on the CCF proved to work efficiently for the detection of potential double-lined spectroscopic binaries. The gain of discovered SB2 binary candidates in the selected DR2 sample of the RAVE survey was small compared to other higher resolution surveys, but still significant. Out of 25,850 examined spectra, we discovered 123 (0.47%) unique SB2 candidate spectra. Only seven were previously known. If we extrapolate this ratio to the entire RAVE sample and assume that the majority of candidate spectra indeed belong to binaries, more than 2000 new SB2 binaries of different kinds will be discovered in the upcoming data releases and will be treated in forthcoming papers. The list of discovered binaries also includes several unusual objects. Among them are a few binary spectra that show signs of chromospheric activity, several close or contact binaries, and a triple system HD 101167.

The detection simulation performed on a large representative sample of synthetic binary spectra showed that the majority of short-period binaries (0.8 days $< P <$ 2 days) are discovered if the luminosity ratio is $\gtrsim$0.3. Assuming that most of the binaries lie along the main sequence the luminosity ratio translates to a mass ratio of $\gtrsim$0.75. At longer periods the detection rate gets progressively smaller, and finally at around 1 yr the probability for detection vanishes.

Fitting the selected sample of binary spectra proved that it is possible to measure Doppler shifts with errors comparable to the RV errors of single stars. The solutions for temperatures and surface gravities from which we derived spectral types were unreliable when fitting the spectra completely unconstrained. We got better results with the assumed main-sequence solutions for both components. There is still room for improvement. Using a more sophisticated model than only a main-sequence assumption could provide even more reliable information on spectral types and also on chemical composition of binaries.

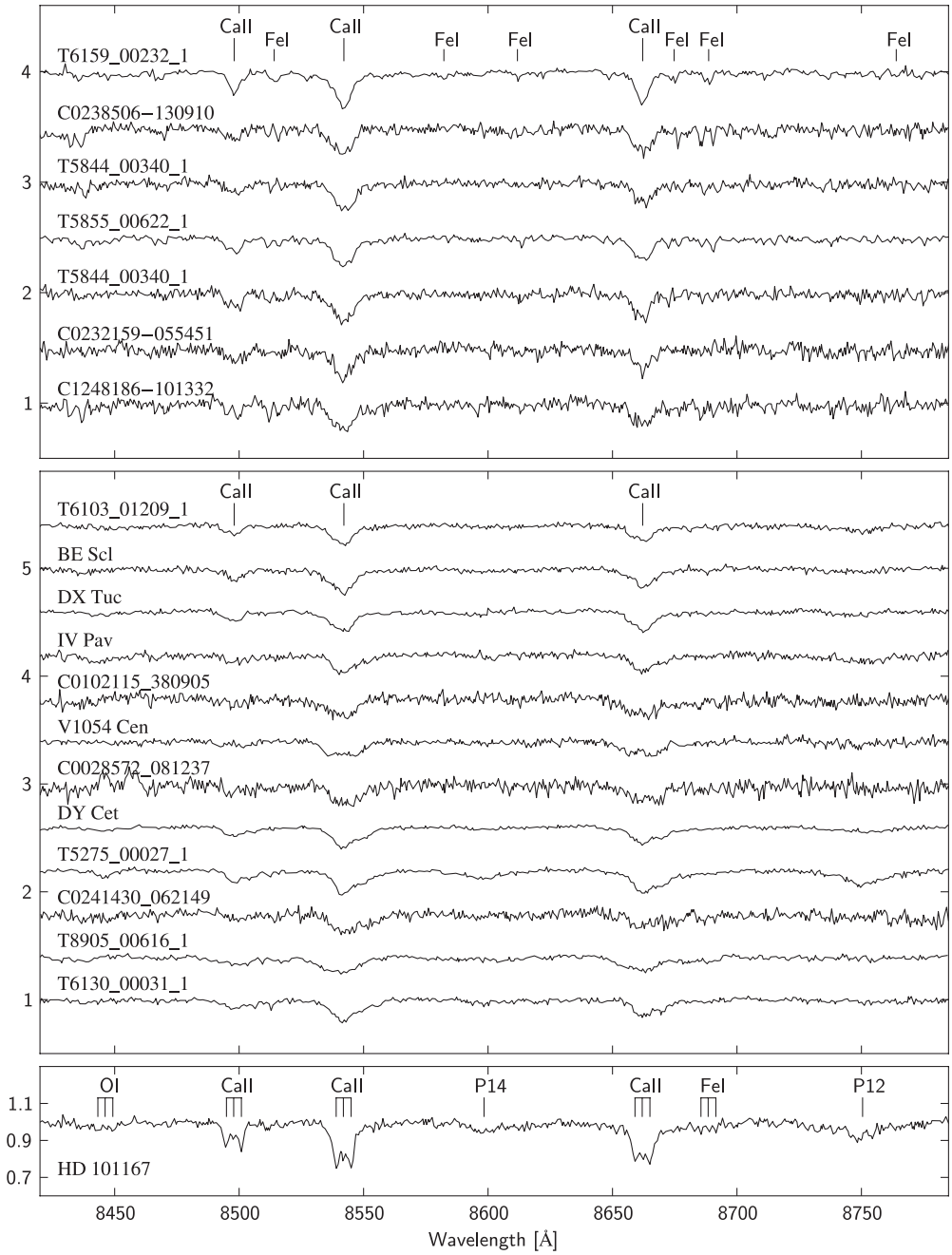

Figure 7. Several peculiar SB2 candidate spectra listed in Table 2. In the first group, there are seven spectra from six objects that show signs of chromospheric activity as observed in RS CVn chromospherically active binaries. All three Ca II lines are shallower compared to other metallic lines. In the second group, there are spectra that can be identified by very wide Ca II lines while all other lines are not visible. The newly discovered ones probably belong to very close binary systems. Triple lines of calcium, iron, and oxygen are clearly visible in the spectrum of HD 101167 in the last plot. The noticeable Paschen series lines (P12 and P14) are too wide and are visible as a single blended line.

Other comparable large-scale spectroscopic surveys are the Geneva–Copenhagen (GC) survey (Nordström et al. 1994) and the Sloan Digital Sky Survey. While the latter is not suited for SB2 observation due to a low resolving power, the former was particularly successful with binary detection. Nordström et al. reported that out of ∼14,000 stars around 34% were either visual or spectroscopic binaries and 510 (∼3.6%) of them showed double lines. The detection of such a high fraction of binaries was possible because of several repeated observations of each object in the longer time span and because of the better resolution of the CORAVEL spectrometer. We ran the detection simulation with the same distribution of re-observations as in the GC survey and the efficiency of SB2 detection was approximately 50% higher than in the case of only one observation per object. Unfortunately, the number of discovered SB2 spectra in the GC survey with velocity difference greater than ∼50 km s^{-1} is not available so a direct comparison of efficiency between the GC and RAVE surveys cannot be done.

The described classification method could also be useful for the forthcoming *Gaia* mission. The spectral data provided by the mission will be very similar to the RAVE data, meaning the method will be applicable without any significant modifications. The enormous scale of *Gaia* observations and the fact that each

object will be observed many times during the lifetime of the mission will yield a large amount of potential new SB2 objects.

We thank the referee, David Latham, for helpful comments that improved the clarity of the text. Funding for RAVE has been provided by the Anglo-Australian Observatory, the Astrophysical Institute Potsdam, the Australian National University, the Australian Research Council, the French National Research Agency, the German Research Foundation, the Istituto Nazionale di Astrofisica at Padova, The Johns Hopkins University, the W. M. Keck Foundation, the Macquarie University, The Netherlands Research School for Astronomy, the Natural Sciences and Engineering Research Council of Canada, the Slovenian Research Agency, the Swiss National Science Foundation, the Science & Technology Facilities Council of the UK, Opticon, Strasbourg Observatory, and the Universities of Groningen, Heidelberg, and Sydney.

REFERENCES

Bate, M. R. 2009, MNRAS, 392, 590
Boeche, C., et al. 2010, A&A, submitted
Breddels, M. A., et al. 2010, A&A, 511, 90
Duquennoy, A., & Mayor, M. 1991, A&A, 1248, 485
Eggleton, P. P. 1983, ApJ, 268, 368
Eker, Z., et al. 2008, MNRAS, 389, 1722
Fernley, J., et al. 1998, A&A, 330, 515
Feroz, F., Hobson, M. P., & Bridges, M. 2009, MNRAS, 398, 1601
Foing, B. H., Crivellari, L., Vladilo, G., Rebolo, R., & Beckman, J. E. 1989, A&AS, 80, 189
Glebocki, R., & Stawikowski, A. 2000, Acta Astron., 50, 509
Heintz, W. D. 1992, ApJS, 83, 351
Koleva, M., Prugniel, P., Bouchard, A., & Wu, Y. 2009, A&A, 501, 1269
Latham, D. W. 2003, in ASP Conf. Ser. 294, Scientific Frontiers in Research on Extrasolar Planets, ed. D. Deming & S. Seager (San Francisco, CA: ASP), 409
Malkov, O. Y., Oblak, E., Snegireva, E. A., & Torra, J. 2006, A&A, 446, 785
Munari, U. 2003, in ASP Conf. Ser. 298, *Gaia* Spectroscopy: Science and Technology, ed. U. Munari (San Francisco, CA: ASP), 55
Munari, U., Dallaporta, S., Siviero, A., Soubiran, C., Fiorucci, M., & Girard, P. 2004, A&A, 418, L31
Munari, U., Sordo, R., Castelli, F., & Zwitter, T. 2005, A&A, 442, 1127
Munari, U., et al. 2008, A&A, 488, 969
Munari, U., et al. 2009, A&A, 503, 511
Nordström, B., et al. 1994, A&A, 418, 989
Seabroke, G. M., et al. 2008, MNRAS, 384, 11
Siebert, A., et al. 2008, MNRAS, 391, 793
Smith, M. C., et al. 2007, MNRAS, 379, 755
Solano, E., Garrido, R., Fernley, J., & Barnes, T. G. 1997, A&AS, 125, 321
Steinmetz, M., et al. 2006, AJ, 132, 1645
Tomasella, L., Munari, U., Siviero, A., Cassisi, S., Dallaporta, S., Zwitter, T., & Sordo, R. 2008, A&A, 480, 465
Torres, G., Andersen, J., & Giménez, A. 2009, A&AR, 18, 67
van Leeuwen, F. 2007, in Astrophys. Space Sci. Libr. 350, *Hipparcos*: the New Reduction of the Raw Data
Veltz, L., et al. 2008, A&A, 480, 753
Yi, S., et al. 2001, ApJS, 136, 417
Zucker, S., & Mazeh, T. 1994, ApJ, 420, 806
Zwitter, T., Castelli, F., & Munari, U. 2004, A&A, 417, 1055
Zwitter, T., et al. 2008, AJ, 136, 421 (Z08)